



Lignin-derived Porous Graphene for Wearable and Ultrasensitive Strain Sensors

Journal:	<i>Journal of Materials Chemistry C</i>
Manuscript ID	TC-ART-03-2022-000953.R1
Article Type:	Paper
Date Submitted by the Author:	30-Jun-2022
Complete List of Authors:	Yang, Shuhong; University of Missouri Ling, Yun; University of Missouri Wu, Qian; University of Missouri Zhang, Hanwen; University of Missouri Yan, Zheng; University of Missouri, Mechanical & Aerospace Engineering; University of Missouri Columbia, Chemical Engineering Huang, Guoliang; University of Missouri, Mechanical and Aerospace Engineering Lin, Jian; University of Missouri, Mechanical & Aerospace Engineering Wan, Caixia; University of Missouri, Biomedical, Biological, and Chemical Engineering

23 stretchable, ultrasensitive strain sensors with applications in human body motion monitoring and
24 sound-related applications.

25 **Keywords:** laser-induced graphene, direct laser writing, lignin, strain sensor, human body
26 motion, vibration detection.

27 **1. Introduction**

28 Strain sensors can be used as wearable and healthcare-oriented electronics for human
29 health monitoring. In general, there are two main categories of human body motion detections,
30 including large scale (bending, jumping, movements of arms and legs, etc.) and small scale
31 (pulse, breath, and other tiny muscle movements).¹⁻⁶ A high-performance strain sensor would
32 require large working range, high sensitivity, long durability, low fabrication cost, etc. Numerous
33 methods, such as carbon nanotube (CNT),⁷⁻⁹ nanoparticles,¹⁰ graphene,^{1, 11} and laser-induced
34 graphene (LIG),¹²⁻¹⁷ have been reported for developing high-performance strain sensor to fulfill
35 the increasing demands for human health monitoring. However, most strain sensors have
36 limitations in sensing. For example, a CNT-based strain sensor with PDMS as an elastomeric
37 substrate had a low gauge factor (0.82~14) although it exhibited excellent stretchability.^{8, 9}
38 Similarly, the strain sensor based on CVD-grown graphene showed high sensitivity in detection
39 of small-scale human motions, but it can only be stretched at 7% strain or below, with a gauge
40 factor only up to 35.¹ Sensor configuration like sandwiched structure can significantly improve
41 gauge factors,^{18, 19} but correlation between signals and applied strains would need to be further
42 improved. Therefore, further efforts would be needed to explore new piezoresistive materials and
43 advance sensor fabrication techniques for developing ultrasensitive, wearable, and stretchable
44 strain sensors with low cost.

45 LIG has been explored as active materials for strain sensor fabrication, as
46 aforementioned. LIG can be facilely synthesized from various precursors using single-step direct
47 laser writing (DLW), exhibiting excellent electrical, chemical, and mechanical properties.^{14, 16, 20,}
48 ²¹ More strikingly, it has intrinsic porous structures which typically cannot be achieved by
49 traditional techniques for graphene synthesis. Such attribute makes LIG a unique active element
50 for strain sensor fabrication. The LIG-based strain sensors particularly derived from polyimide
51 (PI) have been reported to outperform CVD-grown graphene sensors,²² and show high sensitivity
52 to capture various human body motions (e.g., speaking, pulse detection, arm movements).^{12, 16, 17,}
53 ^{23, 24} However, those sensors had the limited detection strain ranges (below 1% strain) and gauge
54 factors below 30 if the LIG-embedded PI film was used for a substrate for sensor fabrication.¹²
55 While stretchable strains can be realized by transferring PI-derived LIG onto an elastomer, the
56 gauge factors were still below 200 with significantly decreased sensitivity in small strain
57 detection. One major reason for comprised sensitivity should be drastically increased sheet
58 resistance (>20 k Ω) associated with LIG transfer.¹⁵ LIG synthesized from other precursors such
59 as cellulose paper was also used to fabricate on-chip, flexible strain sensors; however, the as-
60 prepared sensors had poor stretchability and a very low working range (0~0.3% strain) as well as
61 low gauge factors (only up to 42).²⁵ To fully explore the potential of LIG to be an active material
62 for strain sensors, technical barriers like LIG quality, sensitivity, and transferability would need
63 to be tackled.

64 Among various precursors (polyimide, wood, etc.) explored for LIG,²⁵⁻²⁹ lignin stands out
65 to a unique natural precursor for graphene synthesis given its high-carbon and aromatic
66 structures. Compared to cellulose and hemicellulose, lignin is the most favorable constituent in
67 lignocellulosic biomass for LIG formation. Lignin separated from biomass, so called technical

68 lignin, is more processable than raw biomass like wood to form a suitable substrate for DLW and
69 yield higher quality of LIG. On the other hand, in pulping mills and biorefinery facilities lignin is
70 generated at large quantities (>100 million dry tons annually) as waste streams.³⁰ Therefore,
71 upgrading lignin into graphene-based materials can add additional revenues and be of great
72 significance to paper and pulp and biorefinery industries. As lignin is typically recovered in a
73 powder form from biorefinery, lignin-based films can be made using a binder such as PVA,
74 PEO, and cellulose nanofibers (typically not contributing to LIG formation) to well suit direct
75 laser writing.³¹⁻³³ This strategy would enable mass production of lignin derived LIG as renewable
76 advanced carbon materials via roll-to-roll manufacturing process. Prior studies reported that
77 lignin derived LIG has high potential in energy storage and sensing applications.^{26, 28, 32}
78 However, research on lignin to LIG and subsequent applications is still limited compared to PI, a
79 synthetic polymer precursor. For strain sensing, little research has been done to explore lignin
80 derived LIG as an active material. A recent study reported a strain sensor based on lignin derived
81 LIG/PDMS for human motion monitoring but with low sensitivity as reflected by a quite low
82 gauge factor of 20 because of low LIG quality.³⁴ Therefore, more research efforts are needed for
83 tailoring properties of lignin derived LIG as an excellent piezoresistive material. Further
84 exploration of lignin-to-LIG upgrading pathway would need to address technical barriers to both
85 LIG and lignin-specific precursor. For example, for sensing application, the sensor fabrication
86 could involve LIG transfer from a lignin-based substrate (e.g., film); however, carbon loss, a
87 common issue with LIG regardless of precursors, should be mitigated. Another consideration is
88 to obtain high quality LIG like crystalline graphene since abundant oxygen-containing
89 functionalities in lignin and biomass would contribute to noticeable defects in LIG. To this end,
90 it would be very necessary to tune lasing conditions to ensure LIG quality.

91 In this study, we demonstrated the feasibility to fabricate a stretchable and wearable
92 strain sensor using lignin derived LIG. The LIG was synthesized from kraft lignin by DLW and
93 further transferred onto Dragon Skin™ for sensor fabrication. The LIG transfer was facilitated
94 by a novel technique based on spinning coating coupled with water lifting, without noticeable
95 modification on 3D structure of LIG. The key parameters optimized for lasing included precursor
96 loading, laser power, and defocus distance. The resultant LIG was characterized for
97 microstructure and graphene domains. The fabricated strain sensor showed ultrasensitive
98 response to external stimuli including strains up to 14% and vibrations (5-135 Hz) with high
99 stability. The excellent sensing performance underscored that lignin derived LIG can serve as a
100 highly promising piezoresistive material for detecting tiny deformations induced by strains
101 (below 6%) and vibrations.

102 **2. Methods**

103 **2.1. LIG synthesis**

104 A lignin-based film was prepared by mixing kraft lignin with polyvinyl alcohol (PVA). In
105 brief, PVA (Mw=146,000-186,000) was first dissolved at 9 wt% in deionized (DI) water with
106 continuous stirring at 90 °C for 40 min. Kraft lignin of 0.5, 1.0, or 1.5 g was dissolved in 10 g of
107 2 wt% NaOH solution. Then, the kraft lignin solution was mixed with the PVA solution with 1:1,
108 w/w until clear, dark brown liquid was obtained. The liquid was cast onto a plastic Petri dish
109 with 9 cm in diameter and dried at 35 °C in an incubator with humidity of 25-50% for about 30 h.
110 After drying, the film was peeled off from the Petri dish and attached to a glass slide using
111 adhesive tape for laser writing.

112 A CO₂ laser (30 W, 10.6 μm, Universal Laser Systems VLS3.50 Laser Cutter/Engraver)
113 was used for DLW. The process was conducted under ambient conditions, with 1000 pulses per

114 inch, 10% speed, varying z-axis distance from the focal plane (0.0, 1.0, 2.0, and 3.0 mm), and
115 varying power (20%, 30%, and 40% of the upper limit of laser power setting). An area of
116 $3.0 \times 0.5 \text{ cm}^2$ on the lignin-based film was subjected to laser writing. LIG samples were denoted
117 as LxPy with 2 mm z-axis defocus distance unless stated otherwise, where x stands for the initial
118 mass loading of lignin in a film (i.e., 0.5, 1.0, or 1.5 g) and y for laser power level (i.e., 20%,
119 30%, or 40%).

120 **2.2. Fabrication of strain sensors**

121 A strain sensor was fabricated by transferring LIG onto Dragon Skin™ (Dragon Skin™
122 10 FAST Silicones), an elastomeric substrate. First, Dragon Skin™ was prepared by mixing two
123 prepolymers (Part A: Part B = 1:1, w/w) and then coated to LIG embedded onto the lignin film
124 by a spin coater (Model WS-650MZ-23NPPB) with a spin speed of 3000 rpm and an accelerated
125 speed of 500 rpm/sec. After spinning coating, Dragon Skin™ was cured in a convection oven at
126 35 °C for 30 min. The Dragon Skin™-coated film was then immersed in DI water for about 10
127 min to facilitate the detachment of LIG from the lignin film. The LIG/Dragon Skin™ composite
128 was then dried at 35 °C in a convection oven for 20 min, cut into a dimension of $3.8 \times 0.85 \text{ cm}^2$,
129 and used for the sensor fabrication. The composite was further attached with two copper wires on
130 both ends by conductive epoxy adhesive followed by air drying. Fig. 1 illustrates the sensor
131 fabrication from lignin derived LIG.

132 **2.3. Characterization**

133 LIG embedded onto a film was used for characterization, unless stated otherwise. Raman
134 spectra were acquired on inVia™ confocal Raman microscope at a wavelength of 633 nm. Sheet
135 resistance (R_s) was measured using Pro-4 Four Point Resistivity Systems (Lucas Labs, Gilroy,
136 CA). Morphology of LIG samples was examined using a scanning electron microscope (SEM,

137 FEI Quanta 600 FEG) equipped with a Bruker Quantax 200 Silicon Drift Detector and operated
138 at a 15 kV and 100 pA. High resolution transmission electron microscopy (HRTEM) images
139 were acquired on a JEOL-2100FFEI Tecnai G2 F30 300 kV microscope, and LIG power was
140 sonicated in ethanol for 10 min and imaged. X-ray diffraction (XRD) scanning was conducted
141 for LIG power at 0.02° step size with a scanning rate of 12 s/0.02° using Bruker SMART CCD
142 system.

143 **2.4. Sensing evaluation**

144 Signal patterns for sensing were acquired on an LCR meter (HIOKI IM3523 LCT meter)
145 operated at a DC voltage of 0.1 V. For strain sensing, the sensor was stretched at a varying strain
146 with a rate of 0.2 mm/min by LCR for testing. To detect vibration, a Permanent Magnet Shaker
147 LDS (B&K V203) was used to vibrate the sensor at a frequency of 0-135 Hz or an input voltage
148 of 0-2 V. The invoked amplitudes were proportional to the input voltage. At each level of
149 frequency or input voltage, the strain was kept being vibrated for 10 s. Small-scale human
150 motion detections were also performed, including speaking, eyeball movement, heartbeat (pulse),
151 and breath. The sensor was attached onto a tester's throat, wrist, belly using a biocompatible
152 adhesive gel for signal collecting.

153 **3. Results and Discussions**

154 **3.1. Characterization of lignin derived LIG**

155 Raman spectra reveal that all the LIG samples had three dominant peaks including D, G,
156 and 2D peaks (Fig. S1). Specifically, a D peak at $\sim 1360\text{ cm}^{-1}$ reflects defects and bending of sp^2
157 carbon bonds; a G peak at $\sim 1580\text{ cm}^{-1}$ arises from the first order band of all sp^2 hybridized
158 bonds; and a 2D peak at $\sim 2670\text{ cm}^{-1}$ originates from the second order zone boundary phonons.³⁵
159 High I_G/I_D and I_{2D}/I_G ratios indicate high degree of graphitization and quality graphene,

160 respectively. Laser power showed different effects on the films with different lignin loading. For
161 L0.5, the higher laser power better induced graphene (Fig. S1a). For L1.0, 30% laser power
162 appeared to be sufficient for inducing higher quality LIG with the I_G/I_D and I_{2D}/I_G of 2.7 and 0.77
163 (Fig. S1d&e), respectively, indicating the formation of few-layer graphene with higher quality
164 compared to the counterparts derived from other precursors (e.g., PI, polyetherimide, wood,
165 cellulose paper) and even lignin reported in prior studies.²⁵⁻²⁹ Further increasing lignin loading in
166 the film (L1.5) did not necessarily improve LIG quality regardless of laser power applied (Fig.
167 S1c). In general, high laser power can lead to sufficient carbonization and further
168 graphitization.^{26, 29} However, laser power, if too high, can cause detrimental effects on LIG
169 quality due to severe photothermal irradiation. It should be noted that PVA in the lignin-based
170 composite film would be decomposed and released as gaseous products (H_2O , CO_2 , etc.) during
171 laser scribing rather than contribute to LIG synthesis. The Raman results show that the threshold
172 of laser power for inducing porous graphene would also be related to lignin loading in a
173 substrate. In the case of L1.5, laser parameter would need to be further optimized due to higher
174 lignin loading. In consistence with Raman analysis, the LIG resulting from L1.0 films exhibited
175 at least 2-fold lower R_s than that from the other two films and synthetic polymers-/biomass-
176 based precursors previously reported (Table S1), with the lowest R_s ($4.5 \Omega/sq$) being observed
177 with 30% power level (P30) (Fig. S1f). In addition to optimal laser power, defocused lasing
178 appeared to favor LIG formation compared to focused lasing. Fig. S2 depicts the effects of laser
179 scribing as a function of z-axis defocus when 30% power level was applied. With the z-axis
180 defocus distance increased from 0 (on the focal plane) to 2 mm, the I_G/I_D and I_{2D}/I_G ratios reached
181 the highest values for L1.0 (Fig.S2e). Further increase in the defocus distance to 3 mm led to
182 comprised LIG quality regardless of lignin loading in the films.

183 The LIG resulting from L1.0P30 was further examined for ultrastructure given its
184 impressive Raman spectrum and low R_s . The HRTEM images showed fringe-like patterns of LIG
185 with d -spacing of 0.355 nm between two neighboring (002) planes in graphitic carbon (Fig. 2d).
186 This evidence further supported the presence of graphene and suggested few-layer graphene
187 domain randomly oriented in the LIG. The XRD pattern showed characteristic peaks centering at
188 $2\theta=25.9^\circ$ (assigned to (002) reflection) and $2\theta=42.9^\circ$ (assigned to (100) reflection) (Fig. 2b),
189 with an interlayer spacing of 0.344 nm, indicating that L1.0P30 was well graphitized with high
190 crystallinity. Overall, well-identified graphene domains in L1.0P30 proved successful
191 transformation of lignin into graphene.

192 **3.2. Characterization of LIG/Dragon SkinTM composites**

193 L1.0P30 was selected for the fabrication of strain sensors by transferring the LIG to
194 Dragon SkinTM. LIG transfer was assisted by spinning coating followed by water lifting.
195 Specially, after immersing the whole piece of Dragon SkinTM spin-coated film in water for about
196 10 min, the uncarbonized lignin film was automatically detached from LIG. No residual LIG was
197 found in either the detached lignin film or water, while the transferred LIG showed well retained
198 hierarchical microstructure onto Dragon SkinTM as discussed below. The LIG before and after
199 the transfer was characterized and compared. The SEM images show that rigid and clear lines
200 were formed orderly along with traces of CO₂ laser on the surface of pre-transferred LIG (Fig. 3a
201 & S3a&e). At higher magnification, LIG showed foam-like microstructure as typically observed
202 with LIG synthesis from other precursors (Fig. 3d & S3). The porous structure resulted from
203 rapid release of gaseous molecules (CO₂, H₂O, etc.) as byproducts generated from laser-assisted
204 oxidation and decomposition of lignin film. Water lifting enabled facile transfer of LIG without
205 noticeable loss of LIG. The cross-sectional SEM images also suggested complete transfer of LIG

206 layer onto Dragon Skin™ with similar thickness (115µm) before and after transfer (Fig. 3c&f)
207 and the total thickness of the LIG/Dragon Skin™ composite of ~150µm. Moreover, this finding
208 suggested sufficient infiltration and curing of Dragon Skin™ into interconnected network of
209 LIG. Overall, water lifting method can overcome common issues associated with LIG transfer
210 onto an elastomeric substrate, such as carbon loss and disruption of microstructure. As a result,
211 LIG/Dragon Skin™ can well preserve intrinsic functional properties of LIG and exhibit excellent
212 sensing capability as discussed below.

213 3.3. Sensing strains and vibrations

214 The fabricated strain sensors were evaluated for sensitivity in response to two external
215 stimuli, i.e., strains and vibrations. Like many LIG-based strain sensors, the working mechanism
216 of the proposed strain sensor is proposed to be resistance change caused by increasing gap
217 distance while applying strains. Strikingly, the strain sensor demonstrated ultrasensitivity
218 compared to those based on PI-derived LIG and many other materials (Table S2). For example,
219 the gauge factors of strain sensors based on pristine PI-derived LIG reached only up to 160,
220 about 17% of the maximum value given by the proposed strain sensor.^{12, 15, 36} The R_0 of the strain
221 sensor was around 300 Ω, which made it suitable for low power applications. Fig. 4a depicts that
222 the sensor experienced three stages throughout the stretching and the photo in Fig. 4b shows how
223 the sensor was stretched vertically. Its gauge factor was initially about 100 when the strain was
224 below 4%. The sensor also showed good sensitivity even when a strain was applied as low as
225 0.1% (Fig. S4a). The gauge factor became 160 when the strain was increased from 4% to 9%.
226 When the sensor was stretched further from 9% to 14%, the sensor exhibited a superb gauge
227 factor of ~960. Notably, the signals at three stages had good linearity, i.e., $R^2 > 99$ for Stages
228 1&2 and $R^2 > 98$ for Stage 3. The sensor was also tested for reversibility in a stretch-release

229 cycle for hysteresis test. It showed a low degree of hysteresis (<7%) at 9% strain, suggesting
230 good reversibility (Fig. S4b). Compared to strain sensor based on conventional piezoresistive
231 materials such as CNT and nanowires, the LIG-based strain sensors showed much lower
232 hysteresis degree (Table S2).

233 With the strain range below 9%, the two responding stages can be explained by the fact
234 that with larger strains being applied, the crack between graphene flakes would keep expanding
235 and change into a new junction consisting of reduced conductive paths, leading to the increased
236 gauge factor. The evolution of the crack structure in LIG at different strains applied is also
237 shown in Fig. 4d-g. Within the strain range of 9%-14%, the gauge factor was remarkably
238 increased due to the more enlarged cracks causing more irregular signals. However, when the
239 crack was too large, the electrical connection between responding stages would be broken, with
240 the maximum strain being applied at 14%. The stability of signal was tested by applying
241 different strains (i.e., 2%, 4%, 6%, 9%) (Fig. 4b). For each applied strain, the device kept being
242 stretched for 50 s. It was found that the signals of relative resistance change ($\Delta R/R_0$) were stable
243 and repeatable at a given strain. Compared to start-of-art strain sensors especially based on LIG
244 (Table S2), the proposed strain sensor exhibited significantly improved gauge factor (as high as
245 960) and markedly lower detection limits (as low as 0.1%) for small-scale strain detections (Fig.
246 S4a). Considering excellent sensing linearity, it would be interesting to test and compare with
247 other device configurations like sandwiched structures for ultrasensitivity.^{18, 19} The sensor was
248 further evaluated for stability over 10,000 stretch-release cycles at 4% strain. There were no
249 significant signal fluctuations being observed after 10,000 cycles (Fig. 4c). The sensor's
250 resistance only increased from around 300 to 450 Ω along with ~10% increase in the gauge
251 factor. The findings demonstrated the strain's superb stability of conductive network and

252 reliability for repeated uses, which was shown to be superior to most start-of-art strain sensors
253 fabricated from PI-derived LIG and CNT (Table S2).

254 In addition to strain sensing, the sensor was also shown to be ultrasensitive to vibration,
255 another form of tiny deformation. The resistance change of the strain sensor was continuously
256 monitored throughout the vibration. Fig. 5a&b shows resistance in response to a frequency
257 ranging from 5 to 135 Hz with an increment of 5 Hz when the input voltage was kept at 2V.
258 $\Delta R/R_0$ first increased along with the increasing frequency until reaching the highest value at 85
259 Hz. When the frequency was increased further, $\Delta R/R_0$ drastically dropped to 35% at 100 Hz and
260 then increased. The spike in $\Delta R/R_0$ at 85 Hz suggested that this frequency could be at or near
261 resonant frequency/natural frequency of the sensor. As a result, the sensor can vibrate with a
262 larger amplitude than that at non-resonant frequencies. Larger vibration amplitude can lead to
263 larger cracks and subsequently more significant signal changes. The electrical resistance of
264 sensor was further measured against amplitudes range controlled by input voltages from 0.2-3V
265 when applying a frequency of 85 Hz (Fig. 5c). An excellent linear correlation between $\Delta R/R_0$
266 and input voltage was observed ($R^2 > 99$) (Fig. 5d). These results indicate that lignin derived LIG
267 has exceptional piezoresistive property that can also be explored for sound-related applications.

268 3.4. Sensors for detecting speaking

269 The sensor was used as a speaking detector given the frequency of human speaking
270 ranging from 50 to 300 Hz. Fig. 6&S5 depicts representative strain's performance on detecting
271 human speaking by sensing throat muscle movements and vibrations (Fig. S5a). Swallow, one of
272 typical muscle movements, was also detected, showing distinguishing patterns (Fig. 6a). When
273 one was asked to speak two example words "today" and "beautiful" as well as the whole
274 sentence "Today is beautiful" 4-5 times, the signature peaks corresponding to two individual

275 words were well identified in the whole sentence (Fig. 6b-d). More intriguingly, when the
276 speaking testing was extended to a longer sentence “Laser-induced graphene from lignin-based
277 precursor has many good properties.” three times, the signature patterns of individual words were
278 clearly detected, with good repeatability (Fig. S5b-m&S7a). These findings suggested that the
279 sensor can distinguish tiny deformations caused by speaking, with reliable and repeatable
280 performance. The sensing mechanism for speaking is a combined effect of strains and vibrations.
281 On one hand, the muscle movements of throat during speaking are unique and repeatable, which
282 can be captured as a strain stimulus by the sensor. On the other hand, sound generated during
283 speaking causes vibrations to the sensor. The sensor’s exceptional sensitivity to strains,
284 vibrations, or combined suggests its great potential to be used as a sophisticated speaking
285 detector. One example would be to aid people with disability in speaking by coupling artificial
286 intelligence.

287 **3.5. Sensor for small-scale human motion detection**

288 The sensor’s performance in detecting human motions, including eyeball movement,
289 heartbeat (pulse), breath, and seismocardiography (SCG), was depicted in Fig. 7. The sensor
290 showed excellent and stable responses. For eyeball movement, the sensor was horizontally
291 attached at the lower part of one’s eyes for eye blink, fast eye blinks, looking up, looking down,
292 looking left, and looking right in order, each three times except fast eye blinks. Fig. 7a shows
293 that the strain sensor can provide instant and clear feedback with the unique, stable, and
294 repeatable resistance change patterns for different eye movements. Muscle movements
295 controlling an eyeball to different directions were at tiny scales. Compared to reported eyeball
296 movement sensors.^{37, 38} the proposed strain sensor offers a simpler way to monitor real-time eye
297 movement detection for human health monitoring and virtual reality system.^{38, 39} Furthermore,

298 the strain sensor was attached to one's chest for breath detection, including belly breath (deep
299 breath) and chest breath (normal breath) (Fig. 7b). As breath disorder is usually related to
300 pulmonary diseases (asthma, COVID-19, etc.), the strain sensor's ability to distinguish breath
301 patterns would be highly useful for respiratory system monitoring.

302 SCG is a non-invasive technique used for cardiovascular disease diagnostics by
303 measuring vibrations around chest caused by one's heartbeats. The strain sensor was also
304 evaluated for its performance in SCG signal recording. Fig. 7c depicts the signal patterns to body
305 microvibrations during one cycle of holding breath including systole phrase and diastole phrase.
306 The corresponding region of signal for two phrases as well as their related heart activity are
307 shown in the inset of Fig. 7c. Specially, mitral valve closure (MC), aortic valve opening (AO),
308 and rapid blood ejection (RE) form systole phrase, as well as aortic valve closure (AC), mitral
309 valve opening (MO), and rapid blood filling (RF) from diastole phrase are annotated. The SCG
310 acquired from different positions around the chest including its low part was distinguishing given
311 different structure of human body (Fig. 7c&S6). The signals showed good repeatability across all
312 the testing cycles based on an error band analysis (Fig. S7b). Although the relationship between
313 SCG and electrocardiogram (ECG) is not well understood, recent advances, including more
314 accessible sensors and better algorithms enhanced by machine learning, have demonstrated the
315 potential of SCG in monitoring the health of patient with heart disease.⁴⁰ The proposed strain
316 sensor, which can be facilely fabricated from lignin derived LIG at low cost, can serve the
317 purpose for easy and rapid SCG detection.

318 Pulse wave detection is another key parameter in human health monitoring. As shown in
319 Fig. 7d, the sensor can distinguish the deformations caused by percussion wave (P), tidal wave

320 (T), and diastolic wave (D), which are important indicators to one's cardiovascular health
321 monitoring.⁴¹

322 **4. Conclusions**

323 Lignin-derived strain sensor had excellent performance in detection of small
324 deformations caused by strains and vibrations. It exhibited a large working range for sensing up
325 to 14% strain, with gauge factor as high as 960 and low hysteresis. A good linear relationship
326 between the relative resistance changes and strains was observed. It was also sensitive to
327 vibrations in response to change in frequency and amplitudes. Moreover, the strain sensor can
328 capture tiny deformations based on human speaking, eyeball movements, breath,
329 seismocardiography, and pulses. In all the tests, the strain sensor showed excellent stability and
330 repeatability and was able to generate distinguishing signal patterns of deformations caused by
331 various external stimuli. This work indicated that LIG induced from lignin can be used as an
332 excellent piezoresistive material to fabricate wearable, high-performance, ultrasensitive strain
333 sensors for detection of strain-/vibration-induced deformations toward applications such as
334 healthcare monitoring and sound sensing.

335 **Acknowledgements**

336 This work is supported by the National Science Foundation (Award No. 1933861). The
337 authors thank Domtar Corporation (Fort Mills, South Carolina) for providing kraft lignin.

338 **References**

- 339 1. Y. Wang, L. Wang, T.T. Yang, X. Li, X.B. Zang, M. Zhu, Wang, K. L, Wu, D. H, Zhu and
340 H.W, Wearable and highly sensitive graphene strain sensors for human motion
341 monitoring, *Adv. Funct. Mater.*, 2014, **24**(29), 4666-4670.
- 342 2. D. Son, J. Lee, S. Qiao, R. Ghaffari, J. Kim, J.E. Lee, C. Song, S.J. Kim, D.J. Lee, S.W. Jun,
343 S. Yang, M. Park, J. Shin, K. Do, M. Lee, K. Kang, C.S. Hwang, N.S. Lu, T. Hyeon and

- 344 D.H. Kim, Multifunctional wearable devices for diagnosis and therapy of movement
345 disorders, *Nat. Nanotechnol.*, 2014, **9**(5), 397-404.
- 346 3. C. Pang, J.H. Koo, A. Nguyen, J.M. Caves, M.G. Kim, A. Chortos, K. Kim, P.J. Wang, J.B.H.
347 Tok and Z.A. Bao, Highly skin-conformal microhairy sensor for pulse signal
348 amplification, *Adv. Mater.*, 2015, **27**(4), 634-640.
- 349 4. C.Y. Yan, J.X. Wang, W.B. Kang, M.Q. Cui, X. Wang, C.Y. Foo, K.J. Chee and P.S. Lee,
350 Highly stretchable piezoresistive graphene-nanocellulose nanopaper for strain
351 sensors, *Adv. Mater.*, 2014, **26**(13), 2022-2027.
- 352 5. Z.X. Wu, W.X. Shi, H.J. Ding, B.Z. Zhong, W.X. Huang, Y.B. Zhou, X.C. Gui, X. Xie and J.
353 Wu, Ultrastable, stretchable, highly conductive and transparent hydrogels enabled by salt-
354 percolation for high-performance temperature and strain sensing, *J. Mater. Chem. C*, 2021,
355 **9**(39), 13668-13679.
- 356 6. L. Huang, S. Xu, Z. Wang, K. Xue, J. Su, Y. Song, S. Chen, C. Zhu, B.Z. Tang and R. Ye,
357 Self-reporting and photothermally enhanced rapid bacterial killing on a laser-induced
358 graphene mask, *ACS Nano*, 2020, **14**(9), 12045-12053.
- 359 7. S. Park, M. Vosguerichian and Z.A. Bao, A review of fabrication and applications of carbon
360 nanotube film-based flexible electronics, *Nanoscale*, 2013, **5**(5), 1727-1752.
- 361 8. T. Yamada, Y. Hayamizu, Y. Yamamoto, Y. Yomogida, A. Izadi-Najafabadi, D.N. Futaba and
362 K. Hata, A stretchable carbon nanotube strain sensor for human-motion detection, *Nat.*
363 *Nanotechnol.*, 2011, **6**(5), 296-301.
- 364 9. S.R. Pan, Z. Pei, Z. Jing, J.Q. Song, W.D. Zhang, Q. Zhang and S.B. Sang, A highly
365 stretchable strain sensor based on CNT/graphene/fullerene-SEBS, *RSC Adv.*, 2020, **10**(19),
366 11225-11232.
- 367 10. S. Chen, Y. Wei, X. Yuan, Y. Lin and L. Liu, A highly stretchable strain sensor based on a
368 graphene/silver nanoparticle synergic conductive network and a sandwich structure, *J.*
369 *Mater. Chem. C*, 2016, **4**(19), 4304-4311.
- 370 11. X. Li, R.J. Zhang, W.J. Yu, K.L. Wang, J.Q. Wei, D.H. Wu, A.Y. Cao, Z.H. Li, Y. Cheng,
371 Q.S. Zheng, R.S. Ruoff and H.W. Zhu, Stretchable and highly sensitive graphene-on-
372 polymer strain sensors, *Sci. Rep.*, 2012, **2**, 870.
- 373 12. A.F. Carvalho, A.J.S. Fernandes, C. Leitão, J. Deuermeier, A.C. Marques, R. Martins, E.
374 Fortunato and F.M. Costa, Laser-induced graphene strain sensors produced by ultraviolet
375 irradiation of polyimide, *Adv. Funct. Mater.*, 2018, **28**(52), 1805271.
- 376 13. A. Dallinger, K. Keller, H. Fitzek and F. Greco, Stretchable and skin-conformable
377 conductors based on polyurethane/laser-induced graphene, *ACS Appl. Mater. Interfaces*,
378 2020, **12**(17) 19855-19865.
- 379 14. S.Y. Jeong, J.U. Lee, S.M. Hong, C.W. Lee, S.H. Hwang, S.C. Cho and B.S. Shin, Highly
380 skin-conformal laser-induced graphene-based human motion monitoring sensor,
381 *Nanomaterials*, 2021, **11**(4), 951.
- 382 15. S.Y. Jeong, Y.W. Ma, J.U. Lee, G.J. Je and B.S. Shin, Flexible and highly sensitive strain
383 sensor based on laser-induced graphene pattern fabricated by 355 nm pulsed laser, *Sensors*
384 (*Basel*), 2019, **19**(22), 4867.
- 385 16. L.Q. Tao, H. Tian, Y. Liu, Z.Y. Ju, Y. Pang, Y.Q. Chen, D.Y. Wang, X.G. Tian, J.C. Yan,
386 N.Q. Deng, Y. Yang and T.L. Ren, An intelligent artificial throat with sound-sensing ability
387 based on laser induced graphene, *Nat. Commun.*, 2017, **8**, 14579.

- 388 17. H. Wang, Z.F. Zhao, P.P. Liu and X.G. Guo, Laser-induced porous graphene on
389 polyimide/PDMS composites and its kirigami-inspired strain sensor, *Theor. Appl. Mech.*
390 *Lett.*, 2021, **11**(2), 100240.
- 391 18. M.S. Fan, L. Wu, Y.P. Hu, M.J. Qu, S.T. Yang, P. Tang, L.J. Pan, H. Wang and Y.Z. Bin, A
392 highly stretchable natural rubber/buckypaper/natural rubber (NR/N-BP/NR) sandwich strain
393 sensor with ultrahigh sensitivity, *Adv. Compos. Mater.*, 2021, **4**(4), 1039-1047.
- 394 19. C.W. Li, S.T. Yang, Y. Guo, H. Huang, H. Chen, X.Q. Zuo, Z. Fan, H.W. Liang and L.J.
395 Pan, Flexible, multi-functional sensor based on all-carbon sensing medium with low
396 coupling for ultrahigh-performance strain, temperature and humidity sensing, *Chem. Eng. J.*,
397 2021, **426**, 1385-8947.
- 398 20. R. Rahimi, M. Ochoa, W.Y. Yu and B. Ziaie, Highly stretchable and sensitive unidirectional
399 strain sensor via laser carbonization, *ACS Appl. Mater. Interfaces*, 2015), **7**(8), 4463-4470.
- 400 21. J.J. Park, W.J. Hyun, S.C. Mun, Y.T. Park and O.O. Park, Highly stretchable and wearable
401 graphene strain sensors with controllable sensitivity for human motion monitoring, *ACS*
402 *Appl. Mater. Interfaces*, 2015, **7**(11), 6317-24.
- 403 22. Y. Wang, T.T. Yang, J.C. Lao, R.J. Zhang, Y.Y. Zhang, M. Zhu, X. Li, X.B. Zang, K.L.
404 Wang, W.J. Yu, H. Jin, L. Wang and H.W. Zhu, Ultra-sensitive graphene strain sensor for
405 sound signal acquisition and recognition, *Nano Res.*, 2015, **8**(5), 1627-1636.
- 406 23. L.X. Huang, H. Wang, P.X. Wu, W.M. Huang, W. Gao, F.Y. Fang, N. Cai, R.X. Chen and
407 Z.M. Zhu, Wearable flexible strain sensor based on three-dimensional wavy laser-induced
408 graphene and silicone rubber, *Sensors*, 2020, **20**(15), 4266.
- 409 24. S.D. Luo, P.T. Hoang and T. Liu, Direct laser writing for creating porous graphitic structures
410 and their use for flexible and highly sensitive sensor and sensor arrays, *Carbon*, 2016, **96**,
411 522-531.
- 412 25. B. Kulyk, B.F.R. Silva, A.F. Carvalho, S. Silvestre, A.J.S. Fernandes, R. Martins, E.
413 Fortunato and F.M. Costa, Laser-induced graphene from paper for mechanical sensing, *ACS*
414 *Appl. Mater. Interfaces*, 2021, **13**(8), 10210-10221.
- 415 26. R. Ye, Y. Chyan, J. Zhang, Y. Li, X. Han, C. Kittrell and J.M. Tour, Laser-induced
416 graphene formation on wood, *Adv. Mater.*, 2017, **29**(37), 170221.
- 417 27. Y. Chyan, R.Q. Ye, Y.L. Li, S.P. Singh, C.J. Arnsch and J.M. Tour, Laser-induced
418 graphene by multiple lasing: toward electronics on cloth, paper, and food, *ACS Nano*, 2018,
419 **12**(3), 2176-2183.
- 420 28. W.L. Zhang, Y.J. Lei, F.W. Ming, Q. Jiang, P.M.F.J. Costa and H.N. Alshareef, Lignin laser
421 lithography: a direct-write method for fabricating 3D graphene electrodes for
422 microsupercapacitors, *Adv. Energy Mater.*, 2018, **8**(27), 1801840.
- 423 29. J. Lin, Z. Peng, Y. Liu, F. Ruiz-Zepeda, R. Ye, E.L. Samuel, M.J. Yacaman, B.I. Yakobson
424 and J.M. Tour, Laser-induced porous graphene films from commercial polymers, *Nat.*
425 *Commun.*, 2014, **5**, 5714.
- 426 30. A.J. Ragauskas, G.T. Beckham, M.J. Biddy, R. Chandra, F. Chen, M.F. Davis, B.H. Davison,
427 R.A. Dixon, P. Gilna, M. Keller, P. Langan, A.K. Naskar, J.N. Saddler, T.J. Tschaplinski,
428 G.A. Tuskan and C.E. Wyman, Lignin valorization: improving lignin processing in the
429 biorefinery. *Sci.*, 2014, **344**(6185), 709-720.
- 430 31. F. Mahmood, H. Zhang, J. Lin and C. Wan, Laser-induced graphene derived from kraft
431 lignin for flexible supercapacitors, *ACS Omega*, 2020, **5**(24), 14611-14618.

- 432 32. F. Mahmood, C. Zhang, Y.C. Xie, D. Stalla, J. Lin and C.X. Wan, Transforming lignin into
433 porous graphene via direct laser writing for solid-state supercapacitors, *RSC Adv.*, 2019, **9**,
434 22713-22720.
- 435 33. F. Mahmood, Y. Sun and C.X. Wan, Biomass-derived porous graphene for electrochemical
436 sensing of dopamine, *RSC Adv.*, 2021, **11**, 15410–15415.
- 437 34. C.W. Lee, S.Y. Jeong, Y.W. Kwon, J.U. Lee, S.C. Cho and B.S. Shin, Fabrication of laser-
438 induced graphene-based multifunctional sensing platform for sweat ion and human motion
439 monitoring, *Sens. Actuator A Phys.*, 2022, **334**, 113320.
- 440 35. A.C. Ferrari, J.C. Meyer, V. Scardaci, C. Casiraghi, M. Lazzeri, F. Mauri, S. Piscanec, D.
441 Jiang, K.S. Novoselov, S. Roth and A.K. Geim, Raman spectrum of graphene and graphene
442 layers, *Phys. Rev. Lett.*, 2006, **97**(18), 187401.
- 443 36. T. Han, A. Nag, R.B.V.B. Simorangkir, N. Afsarimanesh, H.R. Liu, S.C. Mukhopadhyay,
444 Y.Z. Xu, M. Zhadobov and R. Sauleau, Multifunctional flexible sensor based on laser-
445 induced graphene, *Sensors*, 2019, **19**, 3477.
- 446 37. S. Mishra, Y.S. Kim, J. Intarasirisawat, Y.T. Kwon, Y. Lee, M. Mahmood, H.R. Lim, R.
447 Herbert, K.J. Yu, C.S. Ang and W.H. Yeo, Soft, wireless periocular wearable electronics for
448 real-time detection of eye vergence in a virtual reality toward mobile eye therapies, *Sci.*
449 *Adv.*, 2020, **6**(11), 1729.
- 450 38. A. Al-Rahayfeh and M. Faezipour, Eye tracking and head movement detection: a state-of-art
451 survey, *IEEE J. Transl. Eng. Health Med.*, 2013, **1**, 2100212.
- 452 39. T.T. Brunye, T. Drew, D.L. Weaver and J.G. Elmore, A review of eye tracking for
453 understanding and improving diagnostic interpretation, *CRPI and Implications*, 2019, **4**, 7.
- 454 40. A. Taebi, B.E. Solar, A.J. Bomar, R.H. Sandler and H.A. Mansy, Recent advances in
455 seismocardiography, *Vibration*, 2019, **2**(1), 64-86.
- 456 41. T.T. Yang, X. Jiang, Y.J. Zhong, X.L. Zhao, S.Y. Lin, J. Li, X.M. Li, J.L. Xu, Z.H. Li and
457 H.W. Zhu, A wearable and highly sensitive graphene strain sensor for precise home-based
458 pulse wave monitoring, *ACS Sens.*, 2017, **2**(7), 967-974.

Figure captions

Fig. 1. Schematic diagram of strain sensor fabrication from lignin derived LIG.

Fig. 2. Characteristics of LIG (L1.0P30). (a) Raman spectrum. (b) XRD spectra of LIG and pristine film (L.0). (c, d) TEM images: scale bars of 20 and 5 nm, respectively.

Fig. 3. SEM images of L1.0P30 before and after transfer. (a, d) Top view before transfer: scale bars of 100 and 20 μm , respectively. (b, e) Top view after transfer: scale bars of 100 and 20 μm , respectively. (c, f) Cross-sectional views before and after transfer, respectively: scale bar of 100 μm .

Fig. 4. Strain sensor's sensitivity to strain. (a) $\Delta R/R_0$ in response to up to 14% strain, with the inset demonstrating the signal change at a strain up to 1%. (b) $\Delta R/R_0$ over the course of testing at different strain levels, with the inset showing the photo of strain sensor stretching. (c) Sensing stability at 4% strain over 10,000 cycles, with the inset showing the first and last 10 cycles (left and right). (d-g) SEM images of evolution of microgap with an increase in strain: scale bar of 100 μm .

Fig. 5. Strain sensor's sensitivity to vibration. (a) $\Delta R/R_0$ at different vibration frequencies (5-135 Hz) when the input voltage for vibration was applied at 2 V. (b) Averaged $\Delta R/R_0$ at different frequencies (5-135 Hz). (c) $\Delta R/R_0$ at different input voltages (0.2-3 V) for vibration when a vibration frequency was applied at 85 Hz. (d) Linear correlation between $\Delta R/R_0$ and input voltages. The photo in (a) shows the testing setup in which the sensor was attached to a permanent magnetic electrodynamic shaker where input voltages were provided.

Fig. 6. Strain sensor working as a speaking detector. (a) $\Delta R/R_0$ of detecting swallow. (b-d) $\Delta R/R_0$ of detecting speaking "beautiful," "today," and "today is beautiful", respectively. The photo in (a) shows the sensor's placement for detecting swallowing and speaking.

Fig. 7. Strain sensor for human motion monitoring. (a) Signal patterns of monitoring eyeball movements. (b) Signal pattern of monitoring belly and chest breath. (c) Signal pattern of seismocardiography. (d) Signal pattern of pulses. The photos show the sensor's placement at different positions for testing. The inset in (c) annotates mitral valve closure (MC), aortic valve opening (AO), and rapid blood ejection (RE) from systole phrase, as well as aortic valve closure (AC), mitral valve opening (MO), and rapid blood filling (RF) from diastole phrase. The inset in (d) shows the signal changes caused by percussion wave (P), tidal wave (T), and diastolic wave (D).

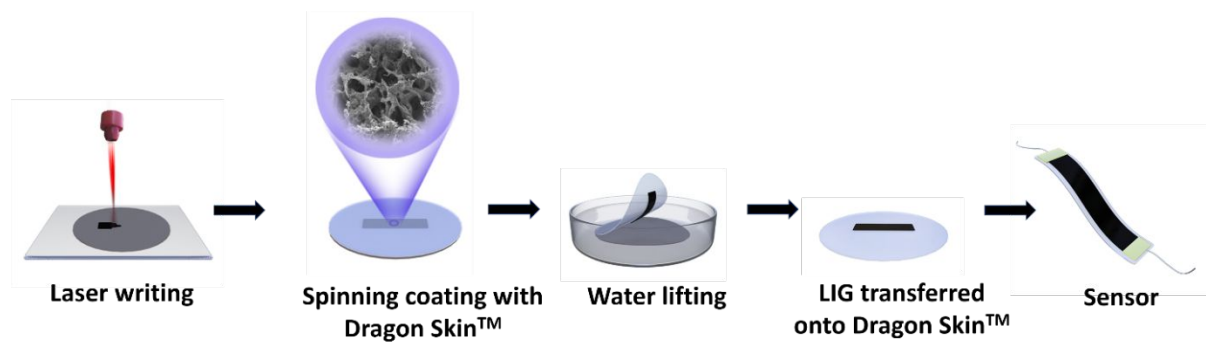


Fig. 1. Schematic diagram of strain sensor fabrication from lignin derived LIG.

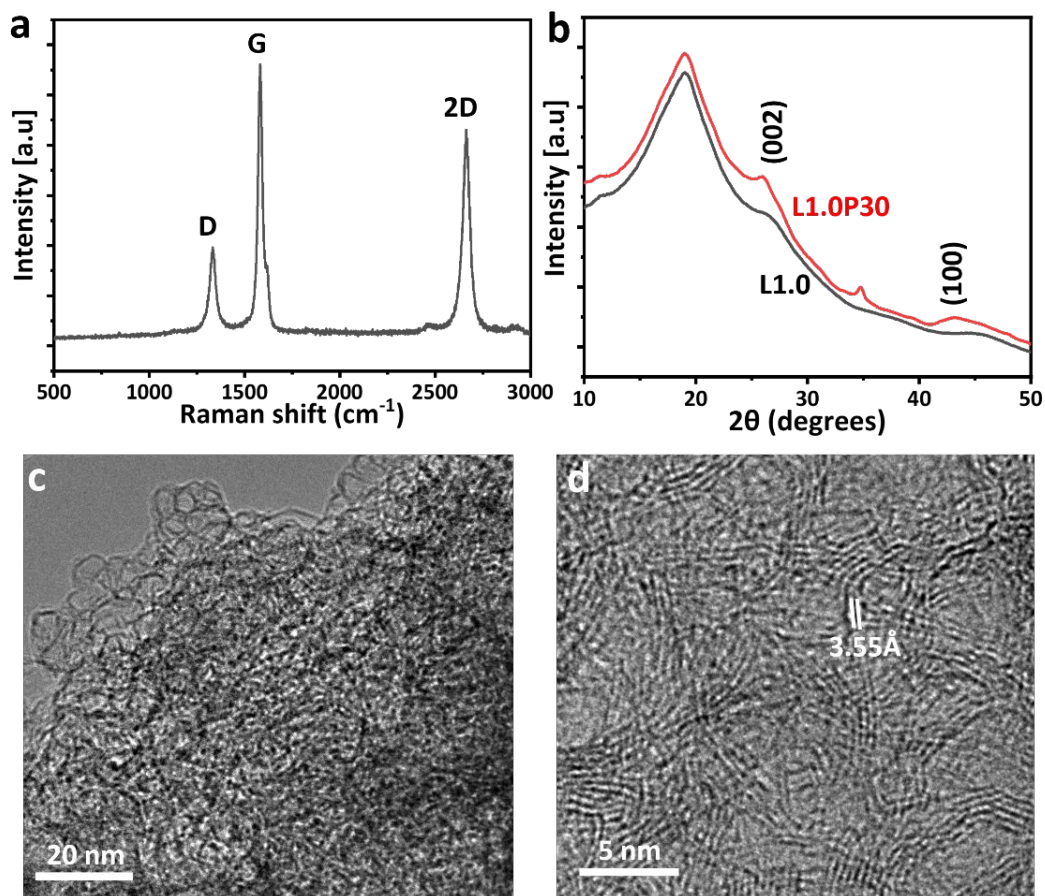


Fig. 2. Characteristics of LIG (L1.0P30). (a) Raman spectrum. (b) XRD spectra of LIG and pristine film (L1.0). (c, d) TEM images: scale bars of 20 and 5 nm, respectively.

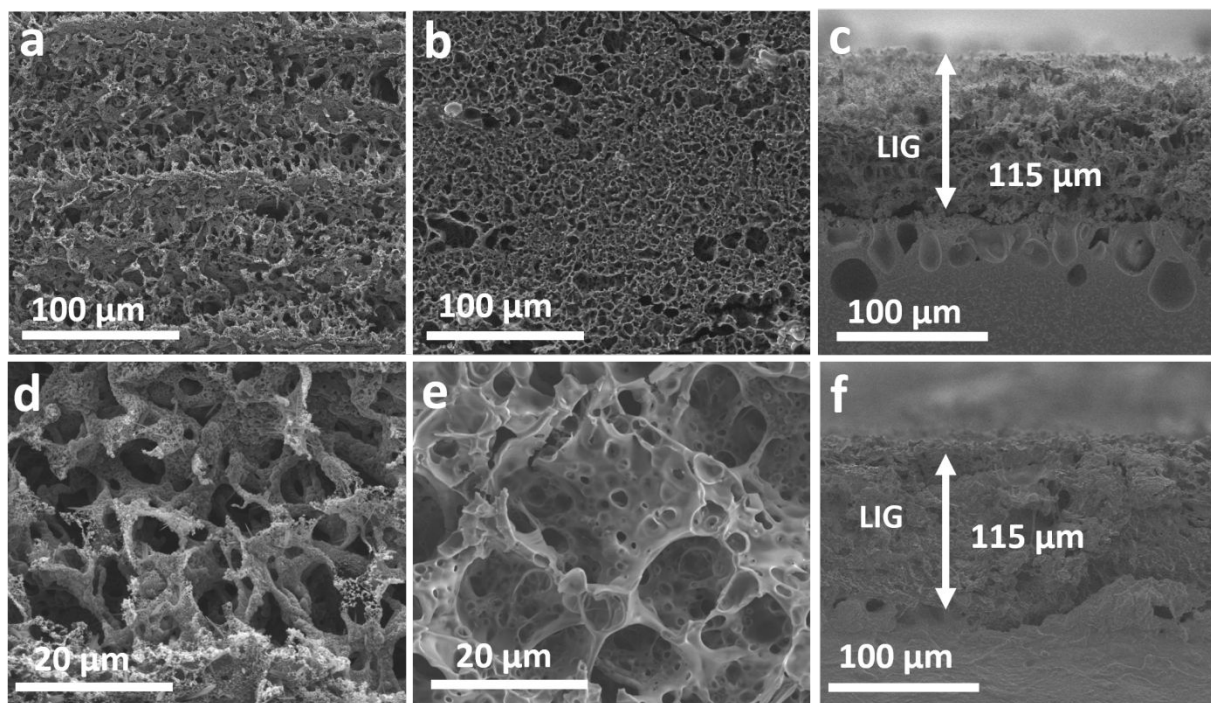


Fig. 3. SEM images of L1.0P30 before and after transfer. (a, d) Top view before transfer: scale bars of 100 and 20 μm , respectively. (b, e) Top view after transfer: scale bars of 100 and 20 μm , respectively. (c, f) Cross-sectional view before transfer and after transfer, respectively: scale bar of 100 μm .

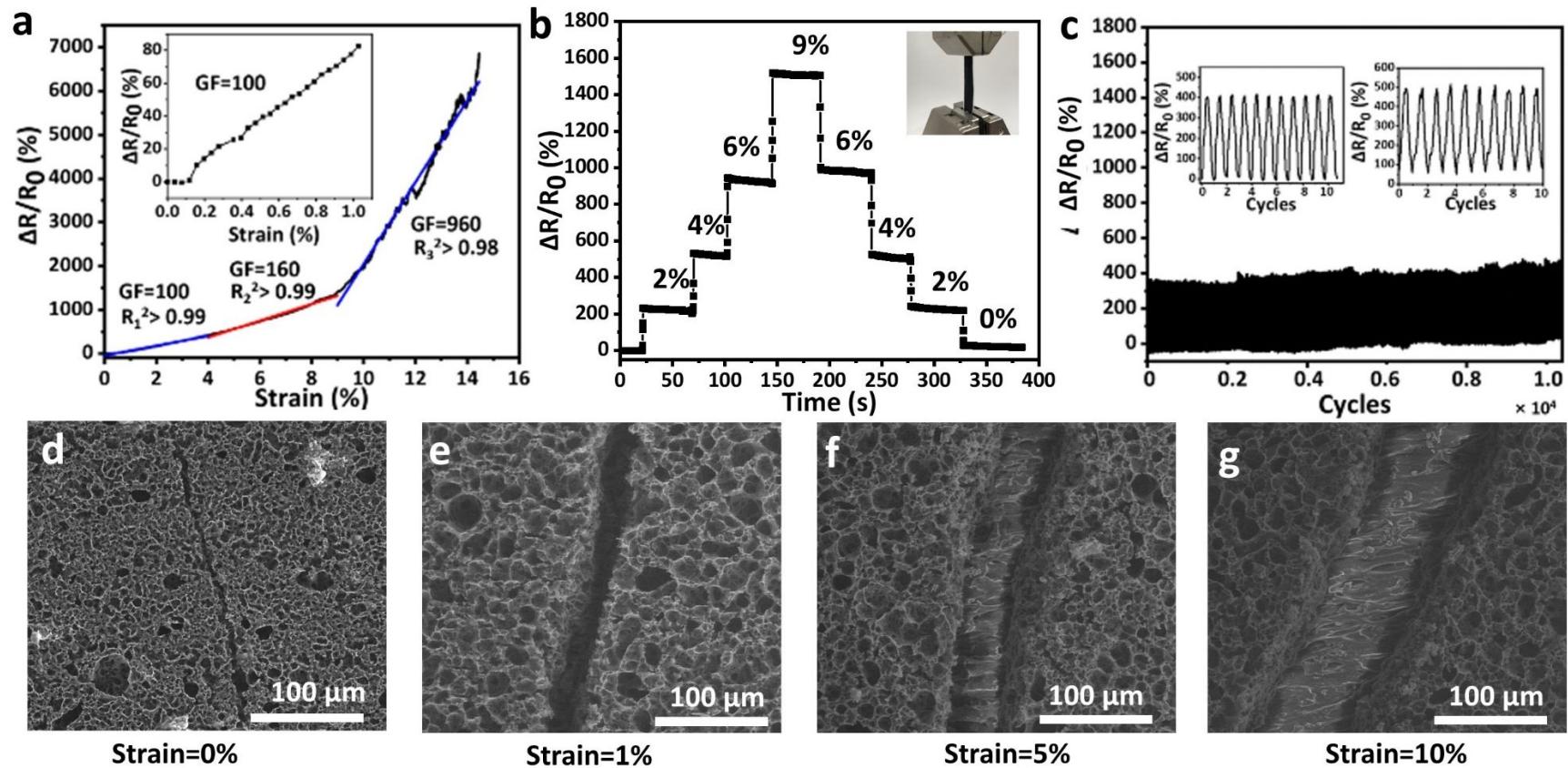


Fig. 4. Strain sensor's sensitivity to strain. (a) $\Delta R/R_0$ in response to up to 14% strain, with the inset demonstrating the signal change at a strain up to 1%. (b) $\Delta R/R_0$ over the course of testing at different strain levels, with the inset showing the photo of strain sensor stretching. (c) Sensing stability at 4% strain over 10,000 cycles, with the inset showing the first and last 10 cycles (left and right). (d-g) SEM images of evolution of microgap with an increase in strain: scale bar of 100 μm .

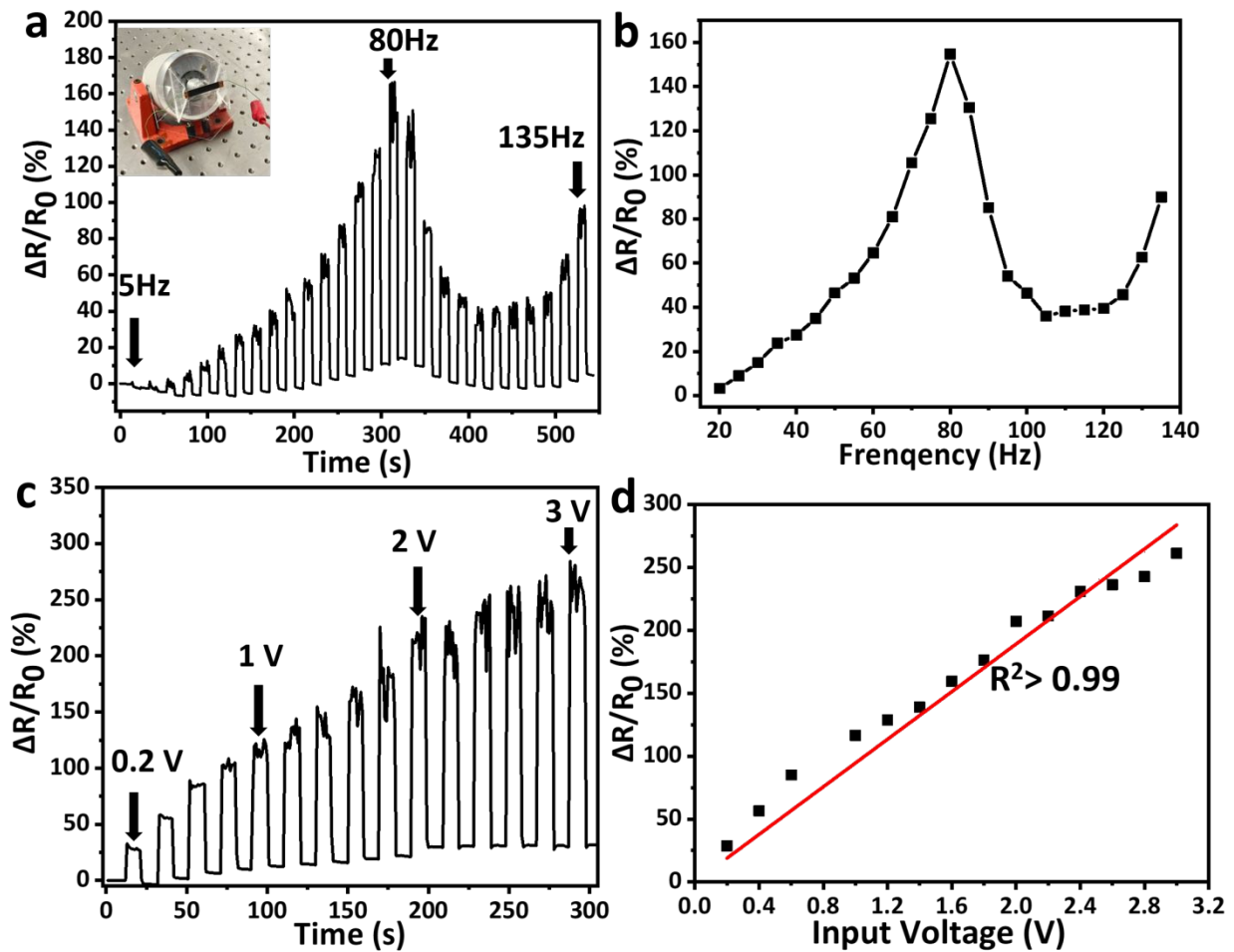


Fig. 5. Strain sensor's sensitivity to vibration. (a) $\Delta R/R_0$ at different vibration frequencies (5-135 Hz) when the input voltage for vibration was applied at 2 V. (b) Averaged $\Delta R/R_0$ at different frequencies (5-135 Hz). (c) $\Delta R/R_0$ at different input voltages (0.2-3 V) for vibration when a vibration frequency was applied at 85 Hz. (d) Linear correlation between $\Delta R/R_0$ and input voltages. The photo in (a) shows the testing setup in which the sensor was attached to a permanent magnetic electrodynamic shaker where input voltages were provided.

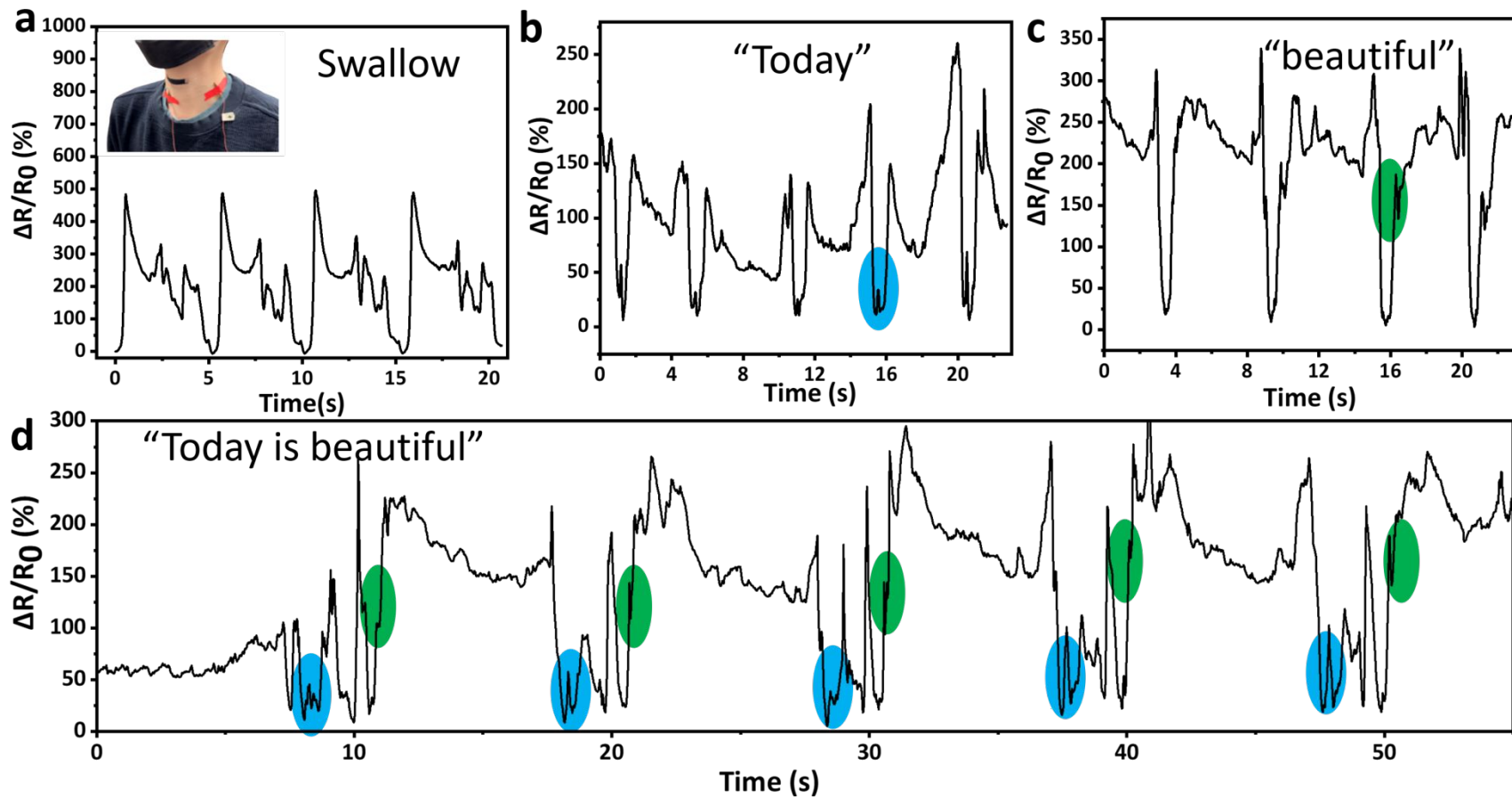


Fig. 6. Strain sensor working as a speaking detector. (a) $\Delta R/R_0$ of detecting swallow. (b-d) $\Delta R/R_0$ of detecting speaking "beautiful," "today," and "today is beautiful", respectively. The blue and green ovals in (b-d) represent signature peaks of the signals during one's speaking "Today" and "beautiful" which were well identified in the whole sentence. The photo in (a) shows the sensor's placement for detecting swallowing and speaking.

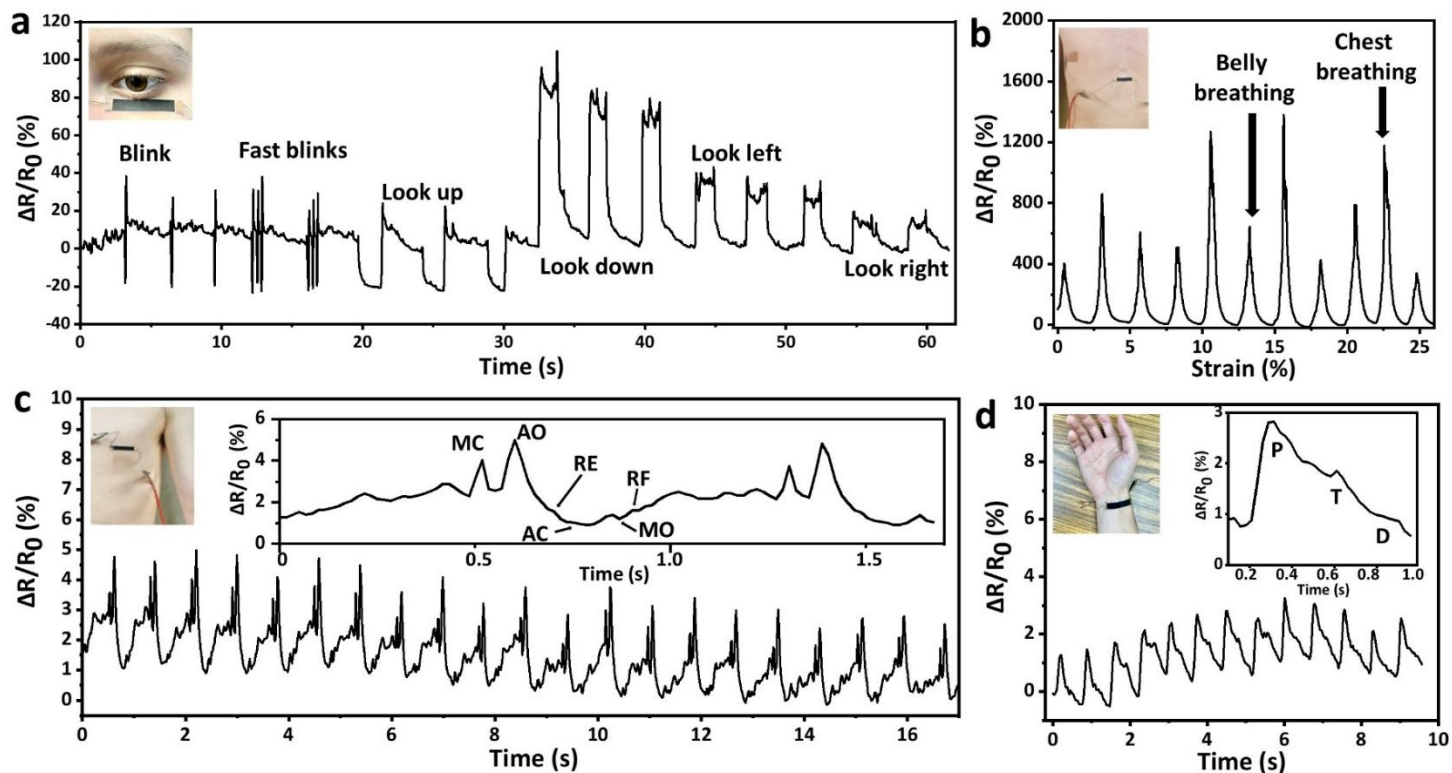


Fig. 7. Strain sensor for human motion monitoring. (a) Signal patterns of monitoring eyeball movements. (b) Signal pattern of monitoring belly and chest breath. (c) Signal pattern of seismocardiography. (d) Signal pattern of pulses. The photos show the sensor's placement at different positions for testing. The inset in (c) annotates mitral valve closure (MC), aortic valve opening (AO), and rapid blood ejection (RE) form systole phrase, as well as aortic valve closure (AC), mitral valve opening (MO), and rapid blood filling (RF) from diastole phrase. The inset in (d) shows the signal changes caused by percussion wave (P), tidal wave (T), and diastolic wave (D).